Medical Image Analysis 34 (2016) 65–81

Contents lists available at ScienceDirect

Medical Image Analysis

journal homepage: www.elsevier.com/locate/media

Seeing the invisible in differential interference contrast microscopy images

Wenchao Jiang, Zhaozheng Yin*

Missouri University of Science and Technology, USA

ARTICLE INFO

Article history:
Received 12 January 2016
Revised 14 April 2016
Accepted 23 April 2016
Available online 3 May 2016

Keywords:
Differential interference contrast microscopy
Image restoration
Motion magnification
Cell segmentation

ABSTRACT

Automated microscopy image restoration, especially in Differential Interference Contrast (DIC) imaging modality, has attracted increasing attentions since it greatly facilitates long-term living cell analysis without staining. Although the previous work on DIC image restoration is able to restore the nuclei regions of living cells, it is still challenging to reconstruct the unnoticeable cytoplasm details in DIC images. In this paper, we propose to extract the tiny movement information of living cells in DIC images and reveal the hidden details in DIC images by magnifying the cells' motion as well as attenuating the intensity variation from the background. From our restored images, we can clearly observe the previously-invisible details in DIC images. Experiments on two DIC image datasets show that the motion-based restoration method can reveal the hidden details of living cells. In addition, we demonstrate our restoration method can also be applied to other imaging modalities such as the phase contrast microscopy to enhance cells' details. Furthermore, based on the pixel-level restoration results, we can obtain the object-level segmentation by leveraging a label propagation approach, providing promising results on facilitating the cell shape and behavior analysis. The proposed algorithm can be a software module to enhance the visualization capability of microscopes.

1. Introduction

As predominantly phase objects, living cells are transparent and colorless under a traditional brightfield microscope, because they do not significantly alter the amplitude of the light waves passing through them, as a consequence, producing little or no contrast under a brightfield microscope Yu et al. (2010). Differential Interference Contrast (DIC) microscopy technique (refer to Chapter 10 in Murphy (2001)) has been widely used to observe living cells since 1950's because it is noninvasive to cells.

The DIC microscope works by splitting a polarized illumination light wave into two component waves that are spatially sheared along a specific shear direction and then recombining the two waves after they pass through *adjacent* locations on the specimen plate. The recombination (*interference*) is sensitive to the phase variation of the two component waves. An adjustable bias retardation is also added into the phase variation. Because the phase variation is caused by the *difference* of the optical path length of two adjacent locations, this microscopy technique is then called "differential interference", and the DIC microscopy converts the optical path length gradient of two locations along the shear direction into intensity variations which are visible to human.

Although the nucleus and some big organelles are visible in DIC microscopy images, there are many cell details which are not obvious in DIC microscopy images such as the cytoplasm and cell membrane, and they are difficult to be observed by human eyes. For example, Fig. 1(a) shows two DIC microscopy image patches and Fig. 1(b) shows the ground truth cell mask obtained by combining the observation from the corresponding phase contrast microscopy images Zernike (1955). Fig. 1(c) is the average segmentation mask by ten human annotators, from which we find that even humankind is likely to ignore the unnoticeable cytoplasm which spreads out into the background, but these hidden details can be informative to analyze cells' shape and behavior. For example, the accurate quantification of cell shape dynamics is important in understanding many biological processes including cell growth Banerjee et al. (2016), cell differentiation Harris et al. (2014) and animal physiology Carter et al. (2016). In this paper, we focus on restoring the invisible (as well as visible) details in DIC microscopy images.

1.1. Related work

Automated image restoration, transforming an observed image that is challenging for direct analysis into a new image that can be

* Corresponding author.
E-mail address: yinz@mst.edu (Z. Yin).

http://dx.doi.org/10.1016/j.media.2016.04.010
1361-8415/

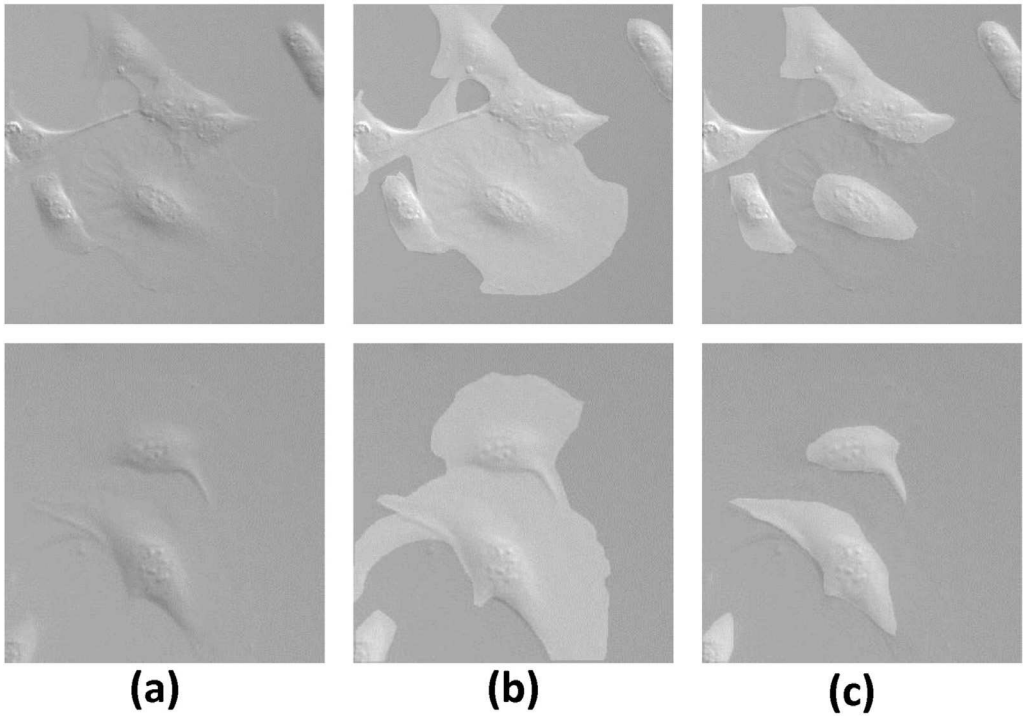

Fig. 1. Challenges in seeing the hidden details in DIC microscopy images. (a). Two original DIC images. (b). The ground truth mask, which indicates where the cells are. (c). The mask indicates where the cells are by ten annotators merely with their naked eyes.

effortless analyzed, has valuable applications in biological experiments, because it may make the segmentation and detection of specimens much easier and greatly facilitate the behavior analysis on specimens. For example, computational imaging models were developed in Su et al. (2012)Yin et al. (2010) to restore microscopy images Li and Yin (2015) Yin et al. (July 2012) or image sequences Yin and Kanade (2011). In Kaakinen (2014), the image restoration improves the performance of cell segmentation by Otsu thresholding, watershed and active contour methods. Multiple microscopy images with various camera exposure settings were also explored in Yin et al. (2014), which restores microscopy images with zero response on non-cell background, facilitating the cell segmentation by thresholding Yin et al. (2015).

The microscopy image restoration is not exactly the same as the general image enhancement that has been widely explored in the natural scene image analysis such as improving global contrast of underwater images Ancuti et al. (2012), estimating the high-resolution images from low-resolution images Ce and Sun (2014), revealing imperceptible temporal variations in frames Wu et al. (2012) and so on. In the enhancement problem, original images are enhanced with sharper edges or higher resolutions. However, in the restoration problem, we would like to clearly observe the cells' details and separate cells from their surrounding background (i.e., the background pixel values are forced to be close to zero while the pixels with cell appearance details are non-zero). Since the general image enhancement techniques cannot be applied to our DIC image restoration problem, we analyze the unique image observations on DIC images and summarize the related restoration work below.

Different from natural scene images, the relief-like images generated by DIC microscopy (e.g., Fig. 2(a)) have the pseudo 3D shadow-cast effect as if the specimens are illuminated from an oblique lighting resource, but this artifact only indicates the *gradient* orientation of specimens' optical path length rather than showing the real topographical structure. This artifact has motivated strong research interests in the DIC microscopy imaging society to restore the direct measurement on specimens' physical properties rather than the indirect interpretation based on gradient signals of the phase variation. We summarize the DIC imaging restoration approaches into three categories below: hardware-based, multi-image based and single-image-based.

Hardware extension was proposed to enhance the original DIC microscope, in order to restore the original signal of phase objects. For example, Arnison et al. (2003) inserted an extra quarter wave plate in the optical pipeline of a DIC microscope and restored the phase objects by varying the bias setting. Shribak et al. (2008) added liquid crystal devices in the original DIC microscope to develop an orientation-independent DIC microscopy technique. These hardware-based restoration methods are very novel and unique, but they might not be accessible to every biology laboratory.

A few approaches were proposed to restore the direct measurement on specimens from multiple DIC images King et al. (2008)Preza (2000)Yin et al. (2011). These approaches either rotate prisms, change bias setting, step the shear azimuth or rotate the cell culture dishes to capture multiple DIC images, which may not be accessible or convenient for the long-term observation on cells in a common biology laboratory.

A major pool of DIC restoration methods is based on microscopy images obtained from the original DIC microscope. The basic techniques employed for microscopy image restoration or segmentation include edge detection, thresholding Neumann, Held, Liebel, Erfle, Rogers, Pepperkok, Ellenberg, 2006), morphological operations Li et al. (2008). These methods often fail when the cells are in low contrast with background. For the purpose of restoration in DIC microscopy images, lines are integrated along the shear direction inspired by the gradient interpretation property of DIC images Kam (1998), but this method introduces streaking artifacts and is sensitive to gradient noise, as shown in Fig. 2(b). Hilbert transform Arnison et al. (2000) and low pass filtering Heise et al. (2005) were explored to improve the line integration result but they can only reduce the streaking artifact to a certain

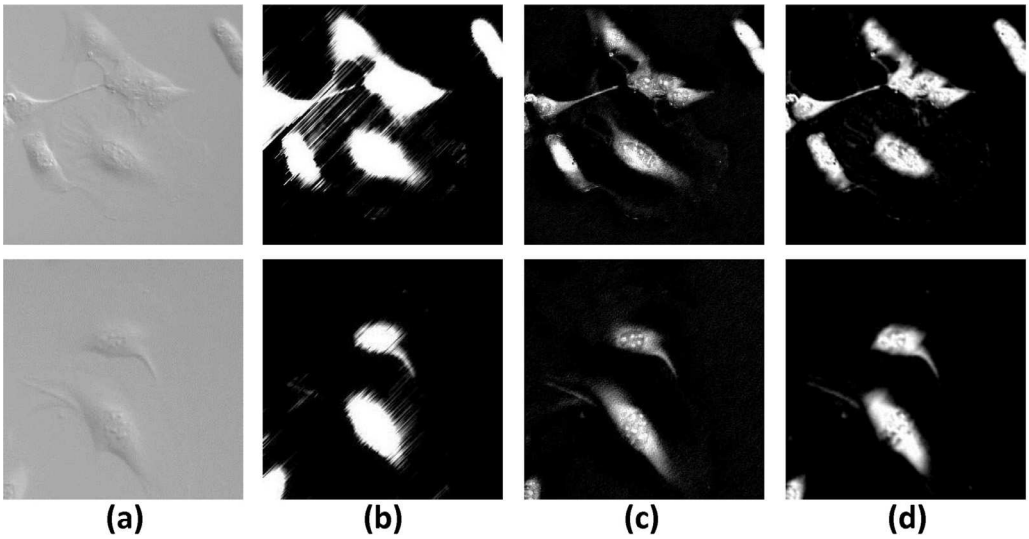

Fig. 2. Challenges in the restoration of hidden details in DIC microscopy images. (a). Two original DIC images. (b). The restoration results by line integration Kam (1998). (c). The restoration results by Wiener filter Heise et al. (2005). (d). The restoration results by preconditioning Li and Kanade (2009).

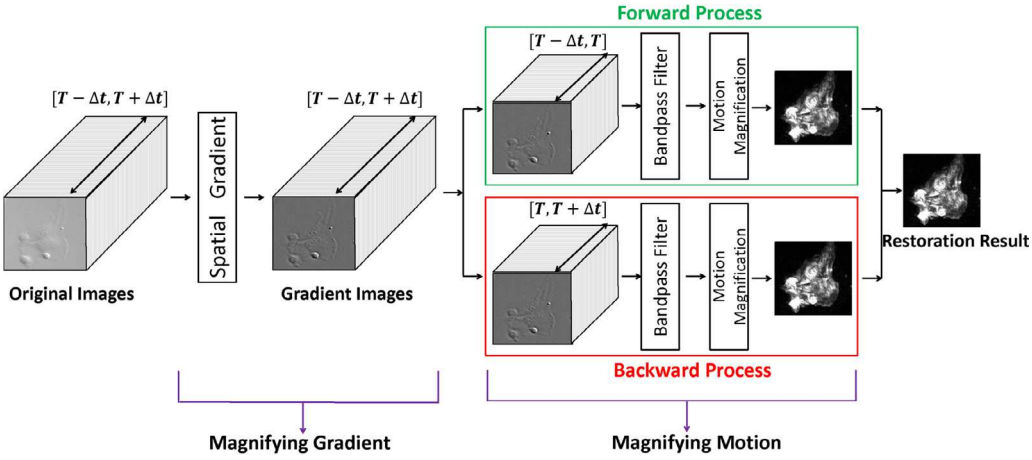

Fig. 3. Overview of our algorithm.

degree. General image processing technologies such as deconvolution by Wiener filter Heise et al. (2005)Van Munster et al. (1997) or Landweber iterations Heise and Arminger (2007) were investigated to restore the direct measurement on phase objects from DIC images, as shown in Fig. 2(c). The performance of the Wiener deconvolution method depends on the prior knowledge of hardware parameters (e.g., the shear direction and bias setting of the DIC microscope) and image noise model. Furthermore, the line integration and Wiener deconvolution methods can only restore the nuclei regions of cells, which have large gradient signals on phase variations, but neither of them can reveal the hidden details on the cytoplasm and cell membrane in the DIC images, which have weak gradient signals on phase variation.

It is worth mentioning that sparse coding based approaches have been popular for biomedical image restoration. A preconditioning approach was proposed in Li and Kanade (2009) where the DIC image was reconstructed by minimizing a nonnegative-constrained convex objective function. A l_1-regularized quadratic cost function was formulated in Yin et al. (July 2012) to restore artifact-free phase contrast images by modeling the phase contrast imaging system. However, when formulating the cost function, the performance of these sparse coding based methods depends on the specific imaging kernel in the data fidelity term and the sparsity level in the regularization term. For example, a computational imaging kernel suitable for restoring dark migration cells may fail to restore other bright cells (e.g., mitotic or apoptotic cells) which have different physical properties Yin et al. (July 2012). Smoothness and sparseness regularization terms are added into the objective function in the preconditioning method Li and Kanade (2009), which ensures the function is well-posed but restricts the restoration of the details of cells, as shown in Fig. 2(d). The sparsity regularization forces many background pixels with small phase variations to be zero in the restored image. Since the cytoplasm within the cell membrane has small phase variations, the corresponding pixels are mistakenly forced to be zero. In this paper, we are interested in seeing the hidden details of cells and the existing sparse coding based approaches are not able to reveal enough detail information of cells.

1.2. Our proposal and algorithm overview

Although the details of living cells in a single DIC image are unnoticeable by human eyes, they are likely to keep moving when we observe them in a continuous series of images, hence we are motivated to think of the following intriguing problem:

Can we extract the tiny movement information of living cells in DIC images and reveal the hidden details in DIC images by magnifying the cells' motion?

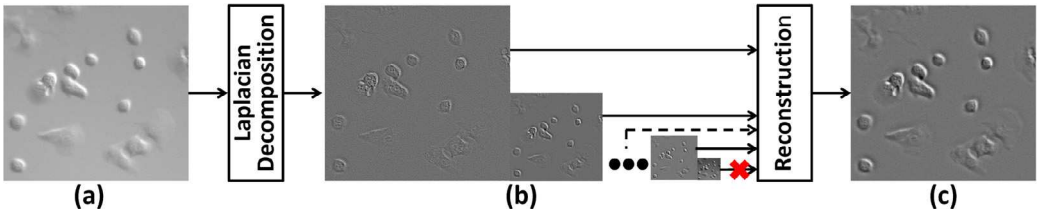

Fig. 4. The flowchart of computing the gradient-magnified image $g(t)$. (a). The original image $f(t)$. (b). The Laplacian pyramid. (c). The image with its spatial gradient information magnified, $g(t)$.

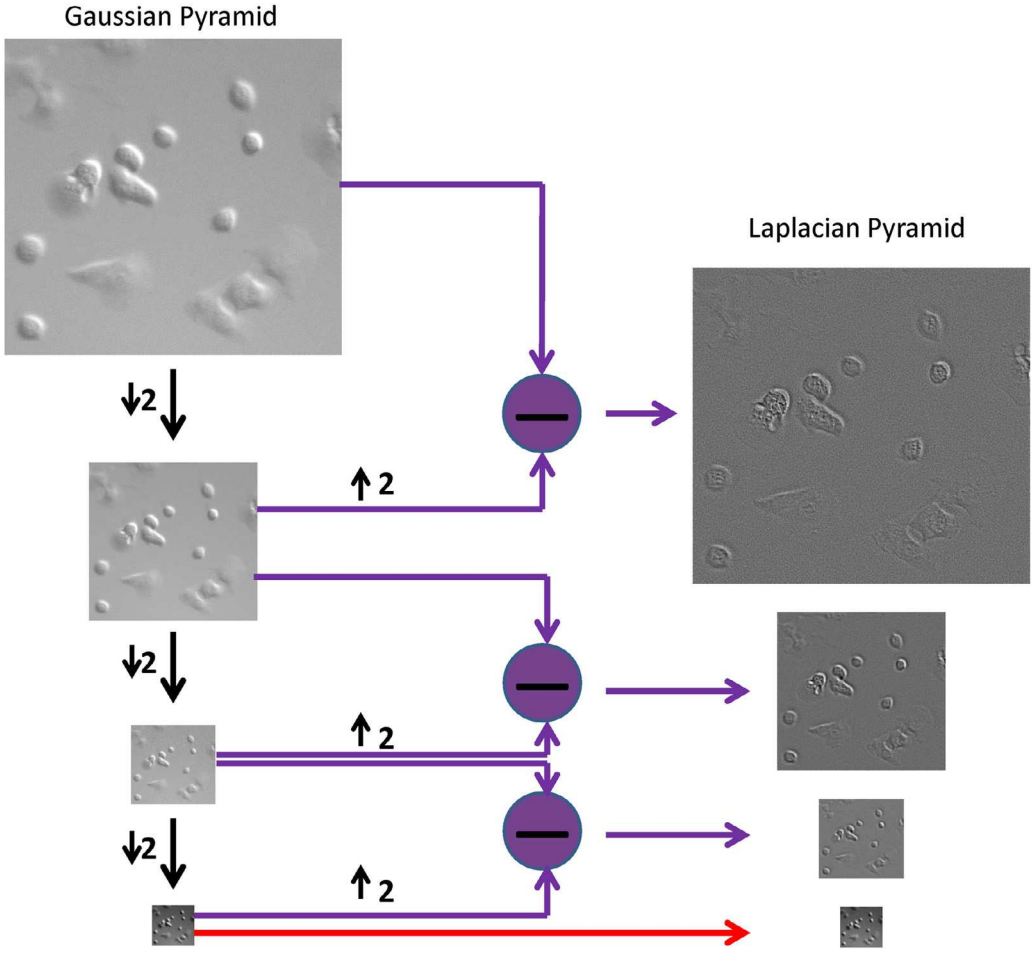

Fig. 5. The process to build the Laplacian pyramid. "↑2" and "↓2" denote upsampling and downsampling the image by the factor of 2, respectively. "⊖" is the subtraction operation of two images. The left side shows how the Gaussian pyramid is computed. On each level, the image is convolved with a Gaussian kernel and scaled down, thus the low frequency information is reserved on that level of the Gaussian pyramid. As the right side shows, the Laplacian pyramid is computed as the difference between each Gaussian pyramid level and its next lower level. Thus, each level of the Laplacian pyramid contains the high-frequency gradient information on that scale. Note that the last level of the Laplacian pyramid contains the low-frequency residual information, which is the direct copy of the last level of the Gaussian pyramid, so we delete the last level of the Laplacian pyramid before our reconstruction in Fig. 4.

In this paper, we propose a motion-based DIC image restoration algorithm, which is an extension of the conference version Jiang and Yin (2015). As shown in Fig. 3, the DIC image at timestamp T is to be restored. We firstly extract and magnify the spatial gradient information of every DIC image within the time sliding window $[T-\Delta t,\ T+\Delta t]$. The intensity values of a pixel location in the gradient images form a time-series signal and we filter it by an ideal bandpass filter to magnify the small motion. The motion is further magnified in forward and backward directions independently in the temporal domain. Finally, the restoration results of two directions by motion magnification are combined to obtain the final restoration result which uncovers the hidden details in the DIC image at timestamp T. Our work is different from the previous work which also considers motion information Hennies et al. (2014)Liu et al. (2014), because we do not rely on cell detection and tracking. Instead, we extract tiny motion on individual pixels and magnify it.

2. DIC image restoration

For simplicity, we denote the original DIC image at timestamp t as $f(t)$, the pixel value of which at position (m, n) is $f(m, n, t)$. Let $v_m(t)$ and $v_n(t)$ denote the motion components at position (m, n) regarding to horizontal and vertical coordinates, respectively. By the first-order Taylor expansion, we have

$$f(m,n,t) = f(m,n,0) + v_m(t)\frac{\partial f}{\partial m} + v_n(t)\frac{\partial f}{\partial n} \tag{1}$$

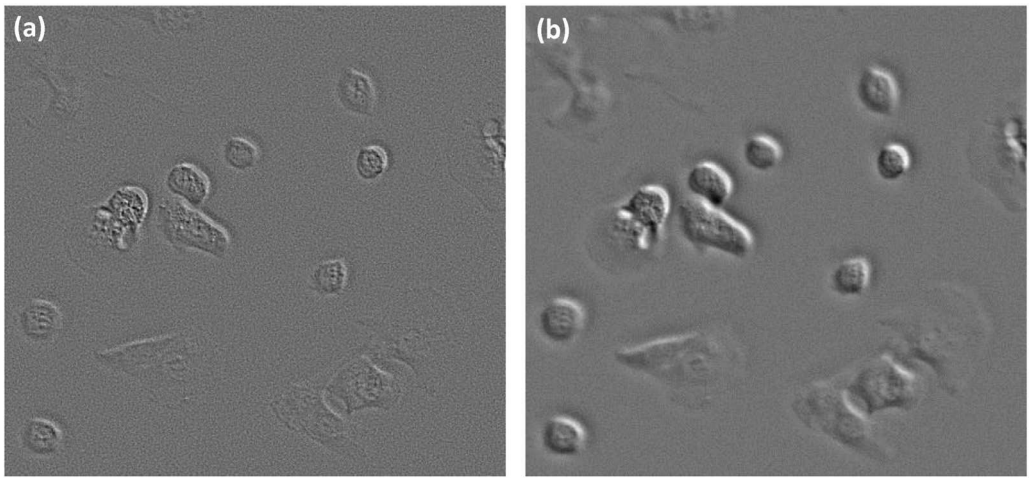

Fig. 6. Spatial gradient magnification. (a). Single level gradient image (the first level of the Laplacian pyramid). (b). Our gradient image by combining multi-levels of the Laplacian pyramid while ignoring the last low-frequency level.

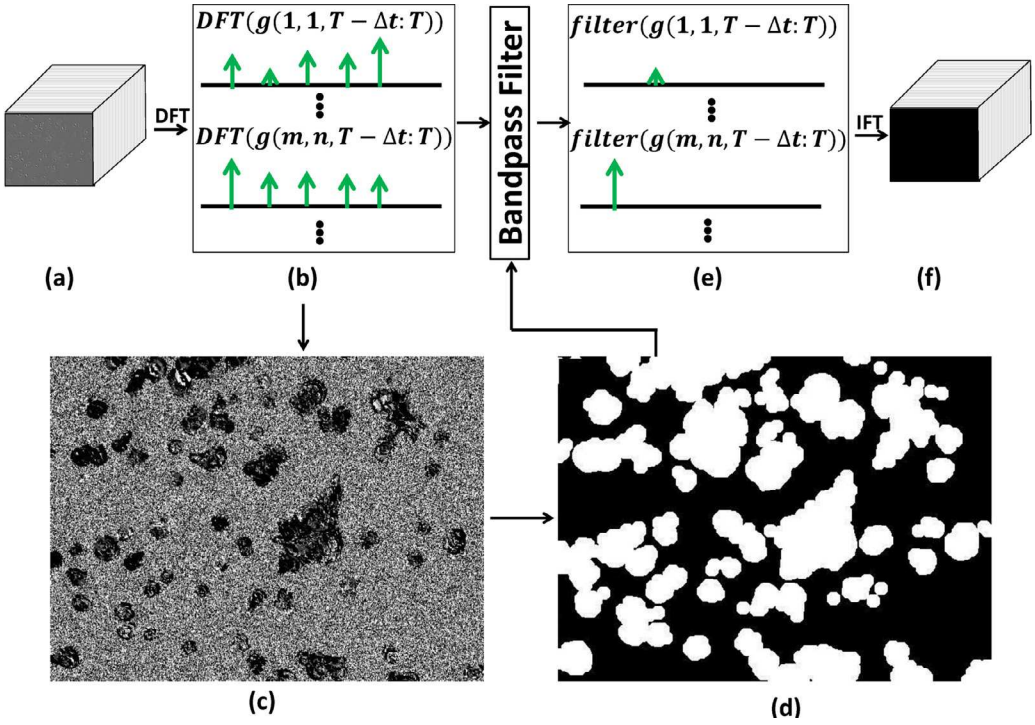

Fig. 7. The flowchart of our bandpass filtering. (a). The images with spatial gradient magnified, $g(t)$'s, with $t \in [T-\Delta t : T]$. (b). The DFT of $g(m, n, T-\Delta t : T)$. (c). The principle frequency image whose pixel value at location (m, n) is the principle frequency of $g(m, n, T-\Delta t : T)$. (d). The bitmask by thresholding the principle frequency image, from which we can know the tentative cell and background regions. (e). The ideal bandpass filtering result with the top being regarded as the background and the bottom being the cell. (f). The motion image $h(t)$, computed by the inverse DFT, indicates the motion of each pixel.

Therefore, the contrast between neighboring pixels in an image sequence (i.e., $f(m, n, t) - f(m, n, 0)$) is determined by both motion information ($v_m(t)$, $v_n(t)$) and spatial gradient information ($\frac{\partial f}{\partial m}$, $\frac{\partial f}{\partial n}$). Given a particular image at timestamp T, $f(T)$, we can restore image details by enhancing the contrast between $f(m, n, T)$ and $f(m, n, T+\Delta t)$ (note that Δt can be positive or negative). According to Eq. 1, we can magnify the contrast by either increasing ($\frac{\partial f(m,n,T+\Delta t)}{\partial m}$, $\frac{\partial f(m,n,T+\Delta t)}{\partial n}$) or increasing ($v_m(\Delta t)$, $v_n(\Delta t)$). This motivates us to build a Laplacian pyramid to accumulate the spatial gradient information at multiple levels to magnify the spatial gradients (Subsection 2.1), design a bandpass filter (Subsection 2.2) and accumulate the motion information in the temporal sliding window (Subsection 2.3 and 2.4) to magnify the tiny motion caused by fine cell structures.

2.1. Magnify the spatial gradient information

Fig. 4 illustrates our process to extract and enhance the spatial gradient information from DIC microscopy images. Given a DIC image $f(t)$ (Fig. 4(a)), we decompose it to several levels by the Laplacian pyramid (Fig. 4(b)) and then reconstruct them by ignoring the last level (Fig. 4(c)).

Fig. 5 illustrates the principle of extracting the spatial gradient information of $f(t)$. Each level of the Gaussian pyramid retains the low frequency information on that level. After building a Gaussian pyramid on an input DIC image, its Laplacian pyramid can be obtained by subtracting each Gaussian pyramid level by the next lower level, reserving the high frequency information on each individual level. Thus, the image on each level of the Laplacian pyra-

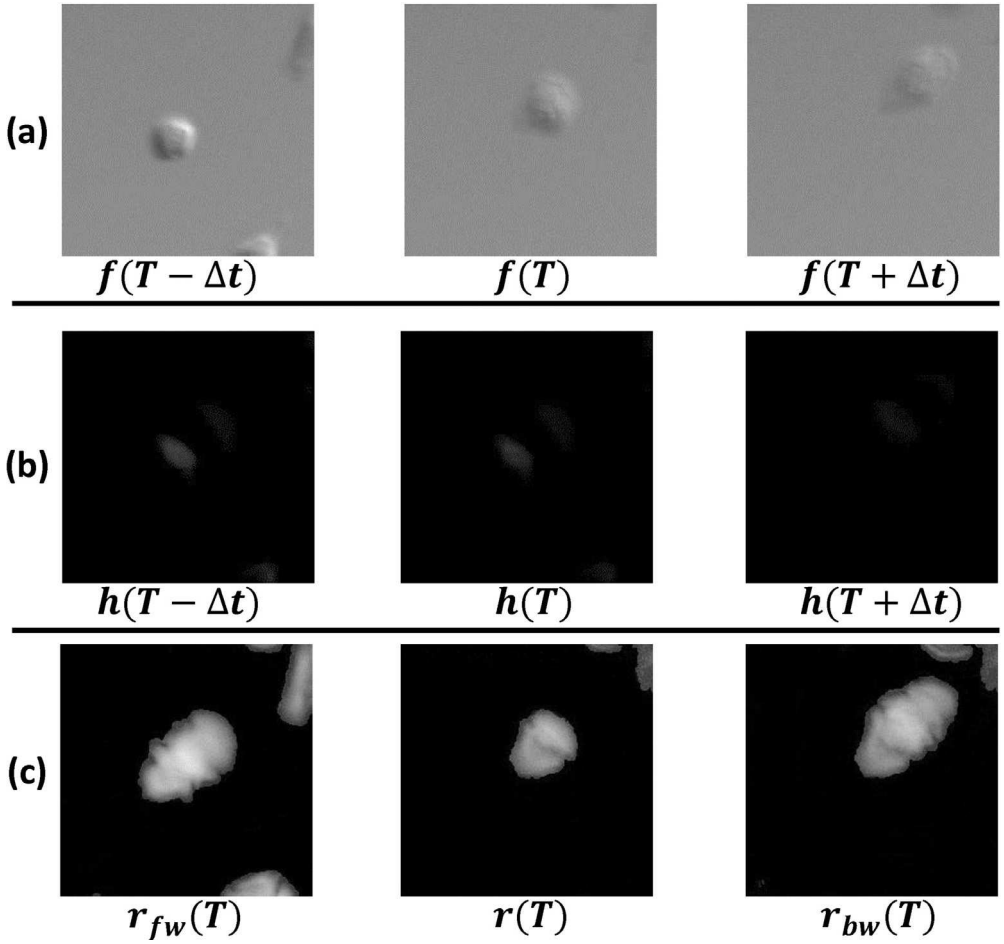

Fig. 8. Motion magnification. (a). Three consecutive DIC images. (b). Motion images of (a) after the bandpass filter. (c). From left to right: accumulated forward motion image, motion image by combining the backward and forward motion images, accumulated backward motion image.

mid can be regarded as the gradient image on that level. However, it is necessary to note that the last level of the Laplacian pyramid is the residual information after Laplacian decomposition, and more accurately, the image on the last level of the Laplacian pyramid is just a copy of the last level of the corresponding Gaussian pyramid, recording the low frequency information, which is the reason that we need to remove the last level before the reconstruction for the gradient (high frequency) magnification.

Fig. 6(b) shows one final result after our gradient magnification. Compared with the single level gradient image, such as the first level of the Laplacian pyramid (Fig. 6(a)), our gradient-magnified image (Fig. 6(b)) that combines several levels reveals more and clearer gradient information about the cells. We denote the gradient-magnified image corresponding to $f(t)$ as $g(t)$ which will be the input of our motion magnification process.

From Fig. 6, another observation of our spatial gradient magnification is that it can increase the signal-to-noise ratio. In the single level gradient image (Fig. 6(a)), the gradient operation amplifies the noise. But, after combining multiple levels in the Laplacian pyramid into a gradient-magnified image (Fig. 6(b)), the gradient information in each level is accumulated or magnified while the noise in each level is relatively reduced or smoothed by the accumulation/averaging.

Note that the spatial gradient information is not sensitive to the signal instability over time. For example, for each image from $f(T-\Delta t)$ to $f(T+\Delta t)$, the pixel value of background is spatially stable (i.e., $(\frac{\partial f}{\partial m}, \frac{\partial f}{\partial n})$ should be small on background pixels), but the image can temporally change because of illumination variations, thus resulting in unwanted temporal motion in the background. Since we consider the spatial gradient information of each image individually, the $(\frac{\partial f}{\partial m}, \frac{\partial f}{\partial n})$ will be small in the background for all images by our method, mitigating the unwanted temporal motion in the background.

2.2. Bandpass filter

Intuitively, motion information $(v_m(t), v_n(t))$ can be extracted by the consecutive image difference of $g(t)$'s, but it is likely to amplify the background noise which is unrelated to cells' movement. We need to retain the tiny motion information of cells, meanwhile inhibiting the unwanted movement information of background pixels.

In this subsection, $g(t)$ is filtered by an ideal bandpass filter pixelwise and the signal-to-noise ratio of each pixel in the temporal domain is increased. The flowchart of our bandpass filtering is shown in Fig. 7, where Fig. 7(a) shows $g(t)$ with $t \in [T-\Delta t, T]$[1]. For each pixel (m, n), we can build a vector $g(m, n, T-\Delta t : T)$ which indicates the pixel value change at (m, n) during the time period of $[T-\Delta t : T]$. The Discrete Fourier Transform (DFT) is then applied to $g(m, n, T-\Delta t : T)$ and Fig. 7(b) shows examples of frequency vs. magnitude on two typical pixel locations. The principle frequency is defined as the frequency with the largest magni-

[1] As shown in Fig. 3, the motion magnification processes towards forward and backward directions in the temporal domain are similar, thus we mainly describe the forward process in this subsection without loss of generality.

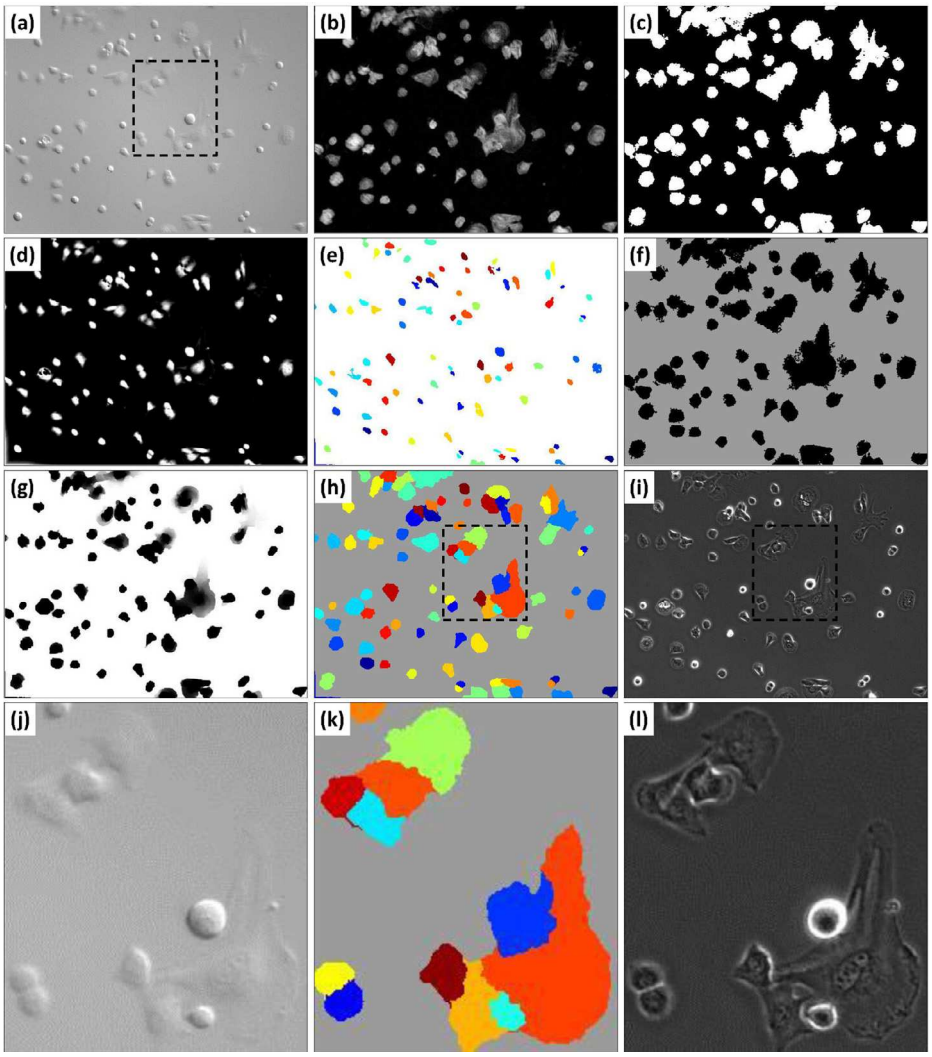

Fig. 9. Object-level cell segmentation based on the restoration. (a). DIC image. (b). Our restored DIC image. (c). Pixel-level cell region segmentation by thresholding the restored image. (d). Restoration by the preconditioning Li and Kanade (2009). (e). Labeled cell pixels (color-coded) obtained from the preconditioning. (f). Labeled background pixels (gray) obtained from our restoration. (g). The background probability of each pixel computed by label propagation. (h). The inferred label of every pixel. (i). The corresponding phase contrast image as a ground truth reference. (j,k,l). The zoom-in subimages of (a,h,i) within the black dash regions, respectively.

tude. As shown in Fig. 7(c), we build a principle frequency map whose pixel value at location (m, n) is the principle frequency of $g(m, n, T - \Delta t : T)$. We observe that in the cells' regions, the principle frequency is lower than that in the background (cell regions and background regions are presented by black and bright regions in Fig. 7(c), respectively). This is because noise variation in the background has a higher frequency (fast changes) but with a smaller range of intensity variation, so people may not notice it. However, the intensity change of a pixel location caused by cell movement has a lower frequency (slow changes) but with a larger range of intensity variation, thus people are possible to observe cell details in continuous DIC images.

The principle frequency map shown in Fig. 7(c) inspires us to tentatively determine cell regions and background. We set all pixel values in the principle frequency map which are larger than the minimum of the principle frequency map as zero, yielding a bitmask that indicates cell regions and background, as shown in Fig. 7(d). The bitmask can *roughly* tell where the living cells are, offering us the hint on where to retain cells' tiny movement and where to inhibit the motion from the background noise.

For each pixel (m, n) in $g(t)$, its movement pattern may not be exactly the same during the time interval $(t \in [T - \Delta t : T])$, thus we design an ideal bandpass filter with the aid of the bitmask to keep the most salient movement of cells as well as the smallest movement in the background. The bandpass filtering increases the contrast between the cell motion and background intensity variation, therefore facilitating the observation on fine details of cells.

For the tentative background regions obtained from Fig. 7(d), the frequency range to be passed in the bandpass filter is set as the frequency corresponding to the *smallest* magnitude, thus all frequency components which are larger are attenuated (rejected). Note that we do not directly set all frequency components of the tentative background pixel as zero, because the tentative foreground and background segmentation in Fig. 7(d) may not be accurate. For the tentative foreground regions obtained from Fig. 7(d), the frequency range to be passed in the bandpass filter is set as the frequency corresponding to the *largest* magnitude, thus only the dominant frequency component related to the cell motion is kept. Fig. 7(e) shows the two filtering results corresponding to Fig. 7(b) with the top being regarded as the background and the bottom being the cell. After the bandpass filtering, we apply the inverse DFT on each pixel's frequency signals to obtain the motion images, $h(t)$.

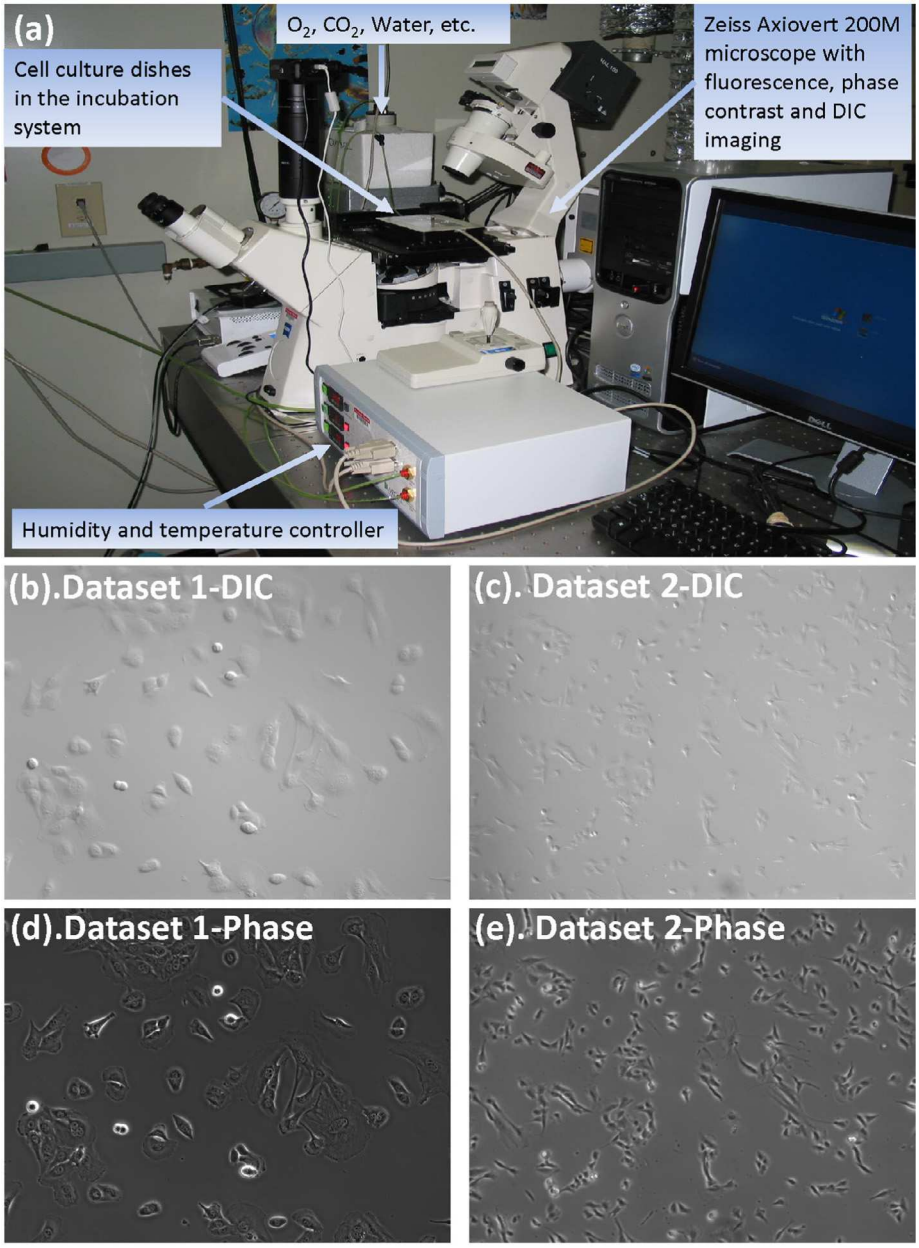

Fig. 10. Experiment setup and dataset samples. (a). Datasets are collected by Zeiss Axiovert 200M microscope. (b). A DIC sample image in Dataset 1. (c). A DIC sample image in Dataset 2. (d). The phase contrast microscopy image corresponding to (b). (e).The phase contrast microscopy image corresponding to (c).

2.3. Motion accumulation

After the aforementioned processes, we obtain the motion image $h(t)$ that includes the movement information of each pixel at timestamp t. Fig. 8(a) shows three original DIC images and Fig. 8(b) shows their corresponding motion images. It is clear that the motion in each individual motion-magnified image is still weak and we need to further magnify it. In this section, we magnify the motion in a temporal sliding window to reveal cell details. This is implemented by the temporally weighted accumulation of motion. The magnification formula for the forward process ($[T-\Delta t, T]$) is defined as

$$r_{fw}(T) = \sum_{t=T-\Delta t}^{T} e^{-\frac{T-t}{\Delta t}} |h(t)|. \tag{2}$$

The magnification formula for the backward process ($[T, T+\Delta t]$) is similarly defined as

$$r_{bw}(T) = \sum_{t=T}^{T+\Delta t} e^{-\frac{t-T}{\Delta t}} |h(t)| \tag{3}$$

where $r_{fw}(T)$ and $r_{bw}(T)$ are the motion-magnified images for $f(t)$ by the forward and backward processes, respectively. $e^{-\frac{T-t}{\Delta t}}$ and $e^{-\frac{t-T}{\Delta t}}$ ensure that the closer the image $h(t)$ is to the target image $h(T)$, the more contribution $h(t)$ makes to $r_{fw}(T)$ or $r_{bw}(T)$. $r_{fw}(T)$ and $r_{bw}(T)$ are shown in the first and third images in Fig. 8(c), respectively. Compared with the motion images in Fig. 8(b), the motion is clearly accumulated/magnified in forward and backward processes.

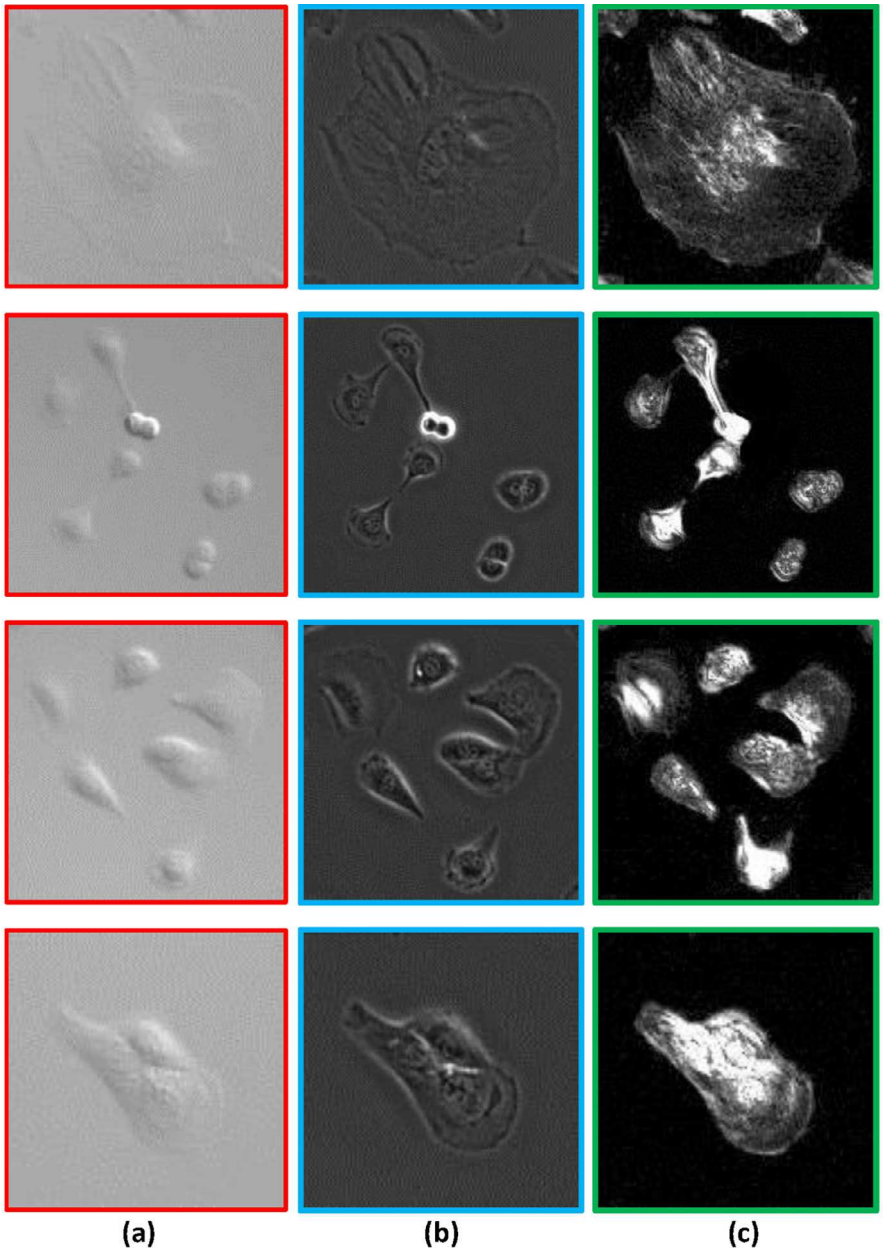

Fig. 11. The proposed restoration method helps us observe the invisible in DIC images. (a). The original DIC images. (b). The corresponding phase contrast images as a ground truth reference. (c). The restored DIC images obtained by our restoration algorithm.

2.4. Combine forward and backward motion images

$r_{fw}(T)$ and $r_{bw}(T)$ accumulate the motion during the temporal period $[T-\Delta t, T]$ and $[T, T+\Delta t]$, respectively. The final restoration image $r(T)$ for the original target image $f(T)$ can be directly defined as the elementwise min-operation on $r_{fw}(T)$ and $r_{bw}(T)$:

$$r(T) = min(r_{fw}(T), r_{bw}(T)). \quad (4)$$

As shown in Fig. 8(a), a cell moves from the image center towards the top-right from $f(T-\Delta t)$ to $f(T+\Delta t)$. Fig. 8(c) shows the forward motion image, combined motion image and backward motion image, respectively. In Fig. 8(c), we observe that if only one direction of motion information is used, there will be artifacts unrelated to the motion in $f(T)$. The artifacts are from the accumulated motion in the past or future DIC images. If we compute the minimum of $r_{fw}(T)$ and $r_{bw}(T)$, the artifacts are removed, leaving the cell details in the current frame only.

3. Object-level cell segmentation based on the restoration

In our restored DIC images, background pixels have values close to zero while cell pixels have non-zero values. Fig. 9(a) and (b) show one DIC image and its restoration, respectively. Segmenting cell pixels from the background pixels can be easily achieved by simply thresholding the restored image, as shown in Fig. 9(c).

After we recover the hidden details of cell cytoplasm within the cell membrane, the pixel-level segmentation in Fig. 9(c) can not separate the clustered cells from each other. We leverage the label propagation method in a supervised graph Su et al. (March 2016) to obtain the object-level segmentation. Given a restored image for the graph-based cell segmentation, first, we need some labeled

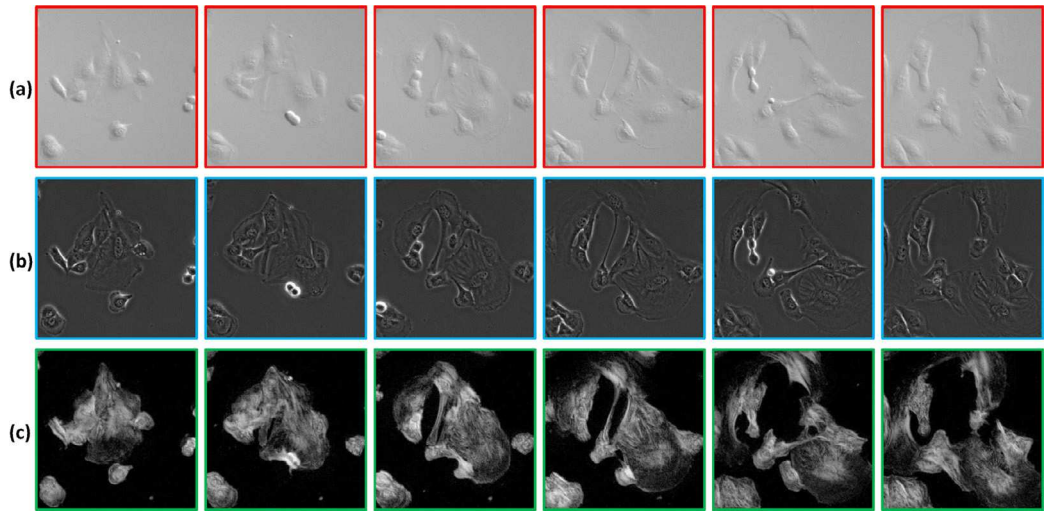

Fig. 12. Seeing more details about cells' behavior over time. (a). Sample DIC images with a time interval of 100 minutes. (b). The corresponding phase contrast microscopy images as ground truth references. (c). DIC restoration images, from which we can analyze the shape change of a cluster of cells over time.

pixel samples from the background and different cells. Since the preconditioning method Li and Kanade (2009) can obtain the cell nuclei regions as shown in Fig. 9(d), we find the local maximums in the preconditioned results and use them (cell nucleus) as the labeled pixel samples for different cells (represented by color blobs in Fig. 9(e)). The labeled pixel samples for the background (represented by gray pixels in Fig. 9(f)) are those pixels whose values in our restoration result (Fig. 9(b)) are zero.

Suppose we have labeled N_c cells and 1 background class, we denote the labeled sample pixels as $\{(\mathbf{x}_l, \mathbf{y}_l)\}_{l=1}^{N_l}$ where N_l is the total number of labeled pixels, $\mathbf{x}_l$ and $\mathbf{y}_l$ are the feature vector and label vector of the lth labeled pixel, respectively. $\mathbf{y}_l$ is a row vector of length $N_c + 1$ with only one entry with the value of one and all other entries being zero. For example, $\mathbf{y}_l = [1, 0, ...0]$ indicates the sample belongs to the background and $\mathbf{y}_l = [0, 1, 0, ...0]$ indicates the sample belongs to the first cell. For all other unlabeled pixels in the restored image, we denote them as $\{(\mathbf{x}_u, \mathbf{y}_u)\}_{u=1}^{N_u}$ where N_u is the total number of unlabeled pixels.

Considering each pixel in the restored image as a node in a regular grid graph and each pixel is linked to its 8-connected neighbors, we compute the link weight as

$$w_{ij} = e^{-\frac{(h_i - h_j)^2}{\lambda}} \tag{5}$$

where h_i denotes the pixel value at pixel i in our restored image. λ is a normalization factor and we choose it as the mean of all possible square costs between neighboring pixels (i.e., $\lambda = mean_{i,j}[(h_i - h_j)^2]$).

Based on the pairwise link weight, we compute the affinity matrix of the graph and permute it into the following structure

$$\mathbf{W} = \begin{bmatrix} \mathbf{W}_{ll} & \mathbf{W}_{lu} \\ \mathbf{W}_{ul} & \mathbf{W}_{uu} \end{bmatrix} \tag{6}$$

where $\mathbf{W}_{ll}$ represents the pairwise link weight between labeled samples, $\mathbf{W}_{lu}$ represents the pairwise link weight between labeled samples and unlabeled samples, $\mathbf{W}_{lu} = \mathbf{W}_{ul}^T$, and $\mathbf{W}_{uu}$ represents the pairwise link weight between unlabeled samples. Then, we compute the Laplacian matrix of the graph as

$$\mathbf{L} = \mathbf{D} - \mathbf{W} \tag{7}$$

where the degree matrix $\mathbf{D}$ is computed as

$$\mathbf{D}(i, i) = \sum_{j=1}^{N_l + N_u} \mathbf{W}(i, j) \tag{8}$$

The label vectors of the unlabeled pixel samples in the graph is obtained by minimizing the following objective function Su et al. (2014)

$$O(\mathbf{Y}_u) = trace([\mathbf{Y}_l; \mathbf{Y}_u]^T \mathbf{L} [\mathbf{Y}_l; \mathbf{Y}_u]) \tag{9}$$

where $\mathbf{Y}_l = [...; \mathbf{y}_l; ...]$ and $\mathbf{Y}_u = [...; \mathbf{y}_u; ...]$ are the label matrices of the labeled and unlabeled pixels, each row of which is an indicator vector. Taking the derivative on $O(\mathbf{Y}_u)$ and setting it to zero lead to the optimal inference for unlabeled pixels as

$$\mathbf{Y}_u^* = -\mathbf{L}_{uu}^{-1} \mathbf{L}_{ul} \mathbf{Y}_l \tag{10}$$

where $\mathbf{L}_{uu}$ represents the submatrix of $\mathbf{L}$ that corresponds to unlabeled pixels and $\mathbf{L}_{ul}$ represents the submatrix of $\mathbf{L}$ that correlates the unlabeled and labeled pixels.

$\mathbf{Y}_u^*$ is a label matrix with the size of $N_u * (N_c + 1)$. Each column of $\mathbf{Y}_u^*$ represents the probabilities of the unlabeled pixels belonging to the specific class. For example, the first column of $\mathbf{Y}_u^*$ represents the background probabilities of unlabeled pixels. Fig. 9(g) shows the background probability of every pixel in the restored image and the labeled background pixels are with probability 1 (white in Fig. 9(g)). For every unlabeled pixel, we determine its class by its maximum value in $\mathbf{y}_u^*$. Fig. 9(h) shows the class labels of all pixels where the color blob represents different cell identities that are consistent with the nuclei regions provided by the preconditioning method (Fig. 9(e)). The phase contrast image is shown in Fig. 9(i) as a ground-truth reference. In Fig. 9(j-l), we crop some sub-images of the full images for the zoom-in visualization. We observe that our restoration can facilitate the cell segmentation, while it is very challenging to segment individual cells from the cell clusters in the original DIC (Fig. 9(j)) or phase contrast images (Fig. 9(l)).

4. Experimental results

In this section, first we describe our experiment setup to obtain the microscopy images. Then, we qualitatively demonstrate how well our restoration method can help visualize the invisible in DIC images. Thirdly, we compare our restoration method based on motion magnification with four other restoration methods both qualitatively and quantitatively. Furthermore, we illustrate that the proposed restoration method can be applied to other imaging modality such as the phase contrast microscopy. In addition to visualizing the hidden details of cells, we further demonstrate that our pixel-level restoration method can benefit the object-level cell segmentation with accurate shapes.

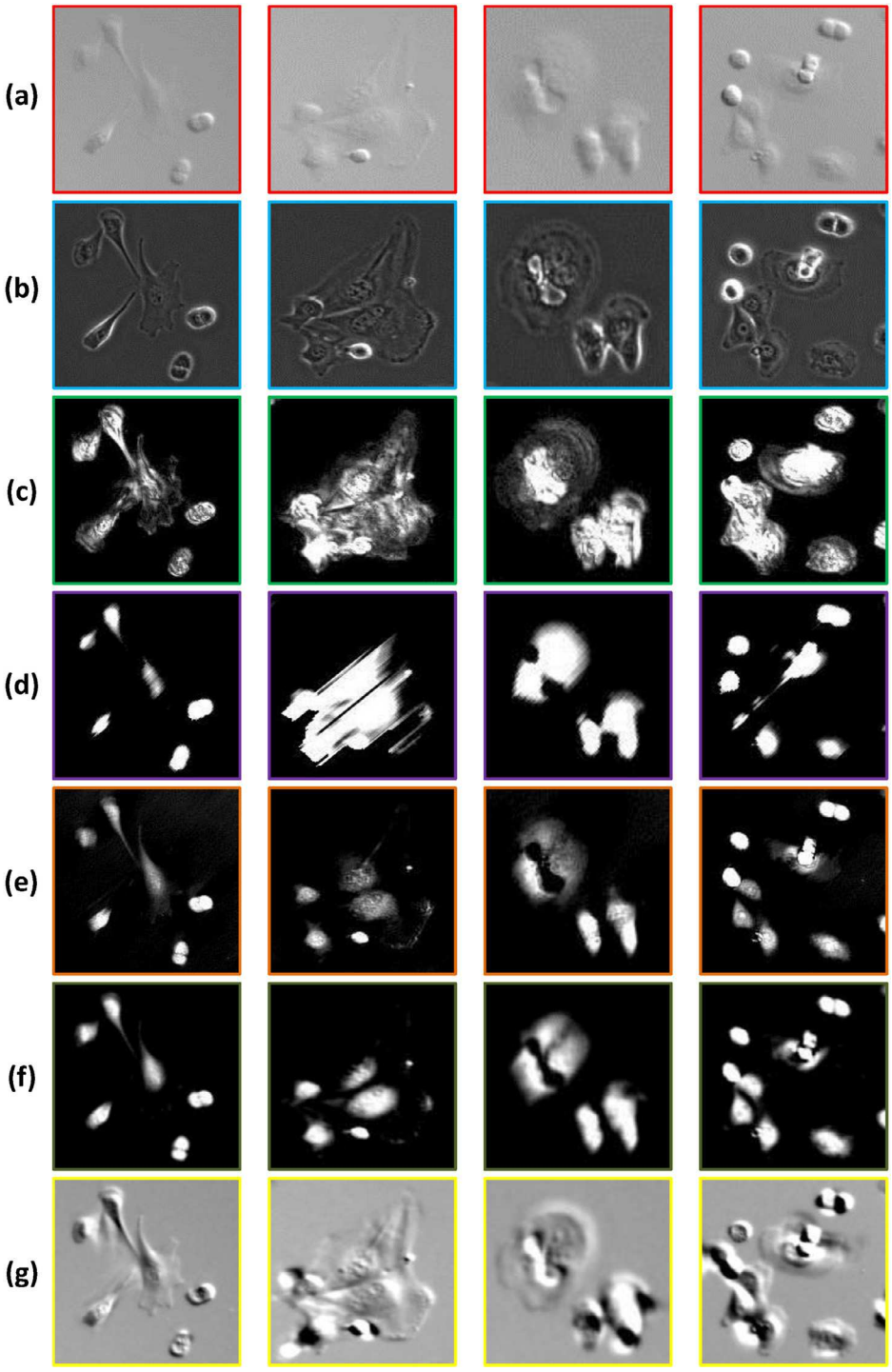

Fig. 13. Qualitative method comparison. (a). The original DIC images. (b). The corresponding phase contrast microscopy images as a ground truth reference. (c). The restored DIC images by our restoration algorithm. (d). The restoration by line integration Kam (1998). (e). The restoration results by Wiener filter Heise et al. (2005). (f). The restoration by preconditioning Li and Kanade (2009). (g). The restoration by Eulerian image magnification Wu et al. (2012).

4.1. Experiment setup

The proposed image restoration algorithm was tested on two sets of Differential Interference Contrast images with the resolution of 1388 × 1040 pixels, which were captured by Zeiss Axiovert 200M microscope (Fig. 10(a)). The cells were cultured in an incubation system placed on the top stage of the microscope which didn't move during the entire experiments and the time-lapse images on living cells were taken every 5 minutes. The first dataset includes 445 DIC images with each image containing about 70 cells (Fig. 10(b) is a sample image). Fig. 10(c) shows a sample image from dataset 2, which includes 500 DIC images and has a wider visual field. Each image in dataset 2 contains about 150 living cells. When labeling the ground truth of cell masks, we found it was very likely to make mistakes if only DIC images are used. To minimize the human error, we captured the phase contrast microscopy images on the same cell dish simultaneously when we captured DIC images. Fig. 10(d) and Fig. 10(e) show the phase con-

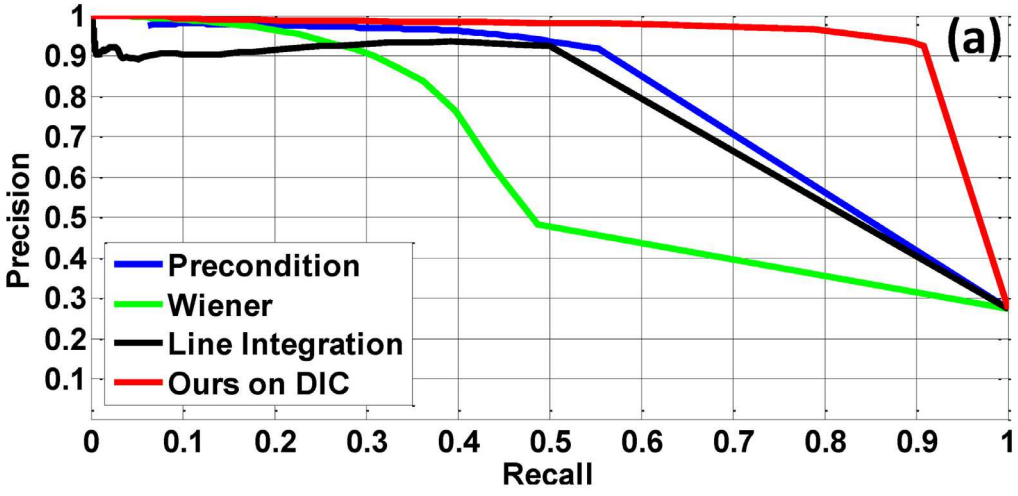

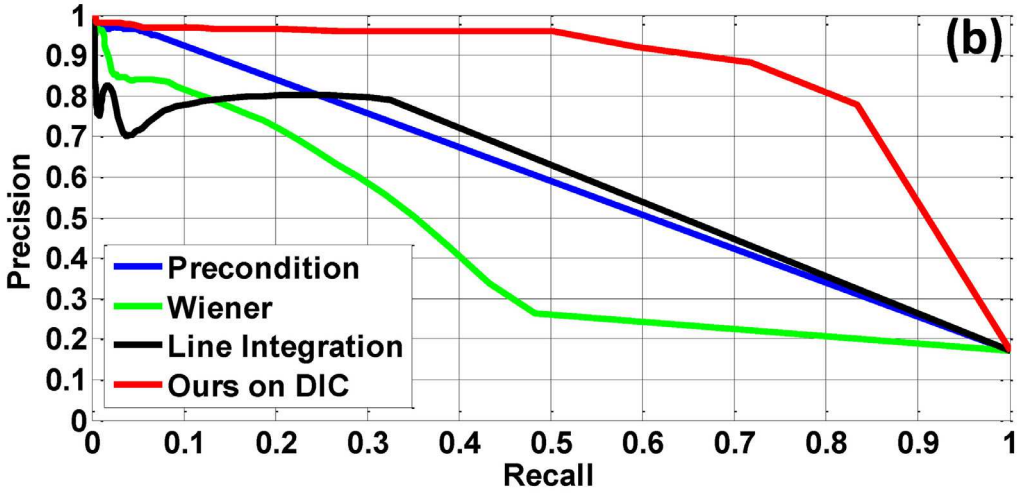

Dataset	(c). Area Under the Curve			
	Precondition	Wiener	Line Integration	Ours on DIC
Dataset 1	0.7392	0.6233	0.7594	0.9438
Dataset 2	0.5847	0.4184	0.5799	0.8577

Fig. 14. The recall vs. precision comparison with other approaches (Precondition: Li and Kanade (2009); Wiener: Heise et al. (2005); Line Integration: Kam (1998)) applied to DIC images. (a). Comparison on dataset 1. (b). Comparison on dataset 2. (c). The area under the recall-precision curve.

trast microscopy images corresponding to the DIC image samples in Fig. 10(b) and Fig. 10(c), respectively. Thus, the ground truth was labeled by combining DIC images and their corresponding phase contrast images.

4.2. Seeing the invisible in DIC images

Fig. 11 shows the proposed restoration algorithm is able to reveal the invisible details in DIC images. In Fig. 11, the images in red or blue boxes are the original DIC images and the corresponding phase contrast images, respectively. Phase contrast images are displayed here to help observe the ground truth. As shown in images in green boxes in Fig. 11, our approach can restore the details such as the cytoplasm of living cells, even though the cytoplasm is spread out and mixed with the background in the original DIC images. With the ability to present more details about living cells, it is easy to observe cells' behavior in the restored image sequence. For instance, Fig. 12 shows some DIC images and their corresponding restoration results on a cluster of cells within a time interval of 100 minutes (the corresponding phase contrast images are provided to help visualize the ground truth). It is clear to observe cells' shape change and their movement, which provides more information for the cell shape and behavior analysis over time.

4.3. Method comparison

We compare the proposed restoration approach with the previous work both qualitatively and quantitatively. Fig. 13(a) and

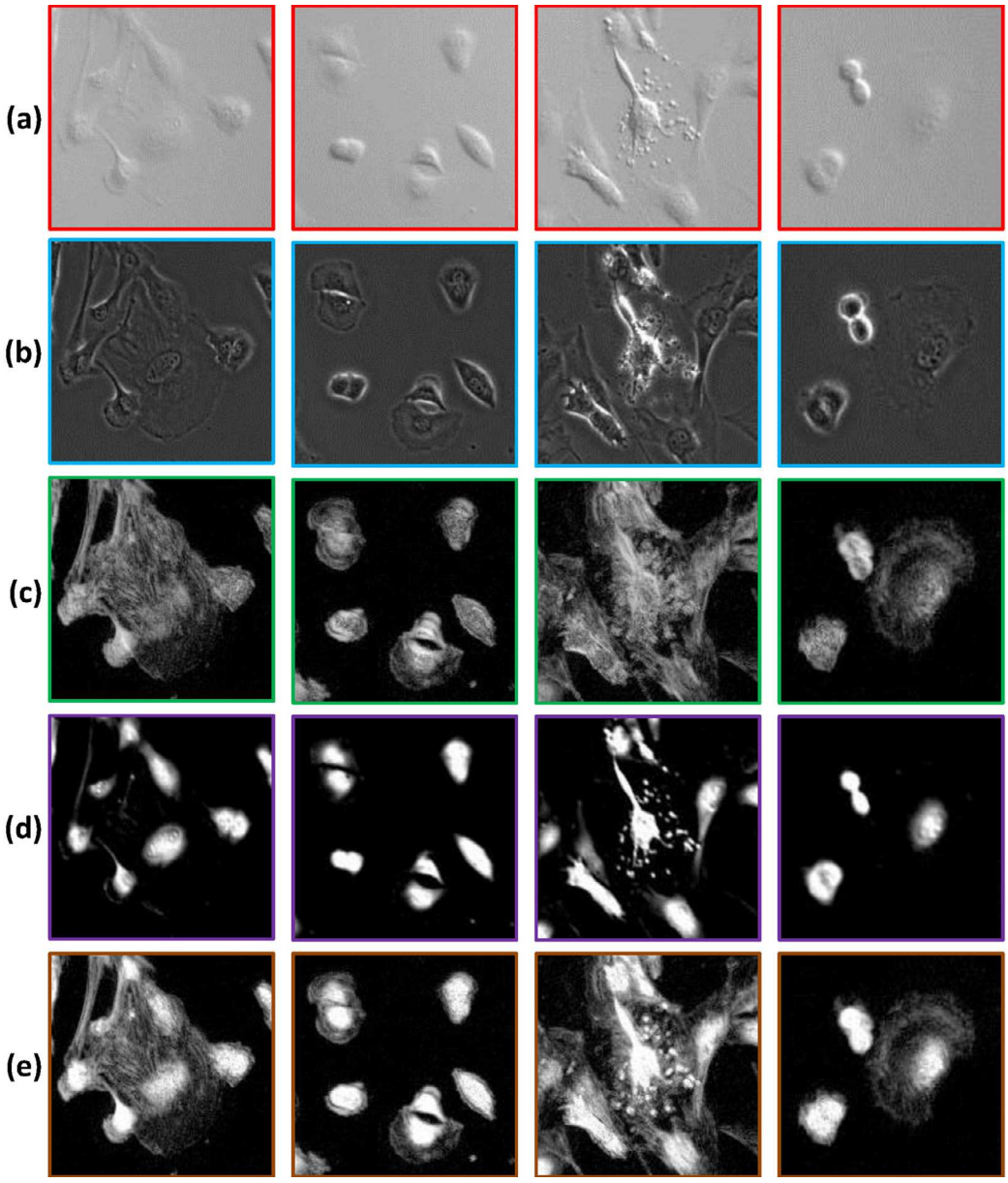

Fig. 15. Advanced visualization by combing the proposed restoration method and preconditioning Li and Kanade (2009). (a). The original DIC images. (b). The corresponding phase contrast microscopy images as ground truth references. (c). The restoration results by our motion magnification method only. (d). The DIC restoration results by the preconditioning Li and Kanade (2009) only. (e). The advanced restoration results by combing our motion magnification method and the preconditioning Li and Kanade (2009).

(b) show some DIC and phase contrast images with different cell sizes. From Fig. 13(c) to Fig. 13(f), we show the restoration results of our restoration method and three existing DIC restoration work on DIC images (Line integration Kam (1998), Wiener filtering Heise et al. (2005), and preconditioning Li and Kanade (2009)). Unlike the three previous work that only reveals the nucleus of living cells and usually misses the cytoplasm, our method reveals more cell details even though they are invisible to naked human eyes.

In addition, as shown Fig. 13(c) and Fig. 13(g), we also compare the performance of our method with a typical image enhancement method proposed in Wu et al. (2012) where the small temporal variations in videos are revealed by the spatial decomposition, followed by the temporal filtering with a known frequency. The method in Wu et al. (2012) can partially display some hidden details of cells, but it also brings artifacts such as the bright and dark regions which are caused by the missmatching between the single unique predefined frequency and the various frequencies of moving cells.

The restored image (a grayscale image with background pixels close to zero and non-zero cell pixel values) enables us to achieve the cell region segmentation (a binary image) simply by using a global threshold. The pixel value range in restored images is normalized to [0, 1], thus we can segment the restoration image with any threshold within [0, 1]. We gradually increase the segmentation threshold by 0.01 from 0 to 1. For each threshold, the average precision and recall for all images in the dataset is computed. Fig. 14(a) and (b) show the recall vs. precision curves on the two datasets by trying different thresholds from 0 to 1 for four methods: our restoration approach, line integration Kam (1998), Wiener filter Heise et al. (2005) and preconditioning Li and Kanade (2009). For each threshold, TP is the number of true positives (cell pixels). FP is the number of false positive pixels. FN is the number of false negative pixels. Thus, precision is defined as

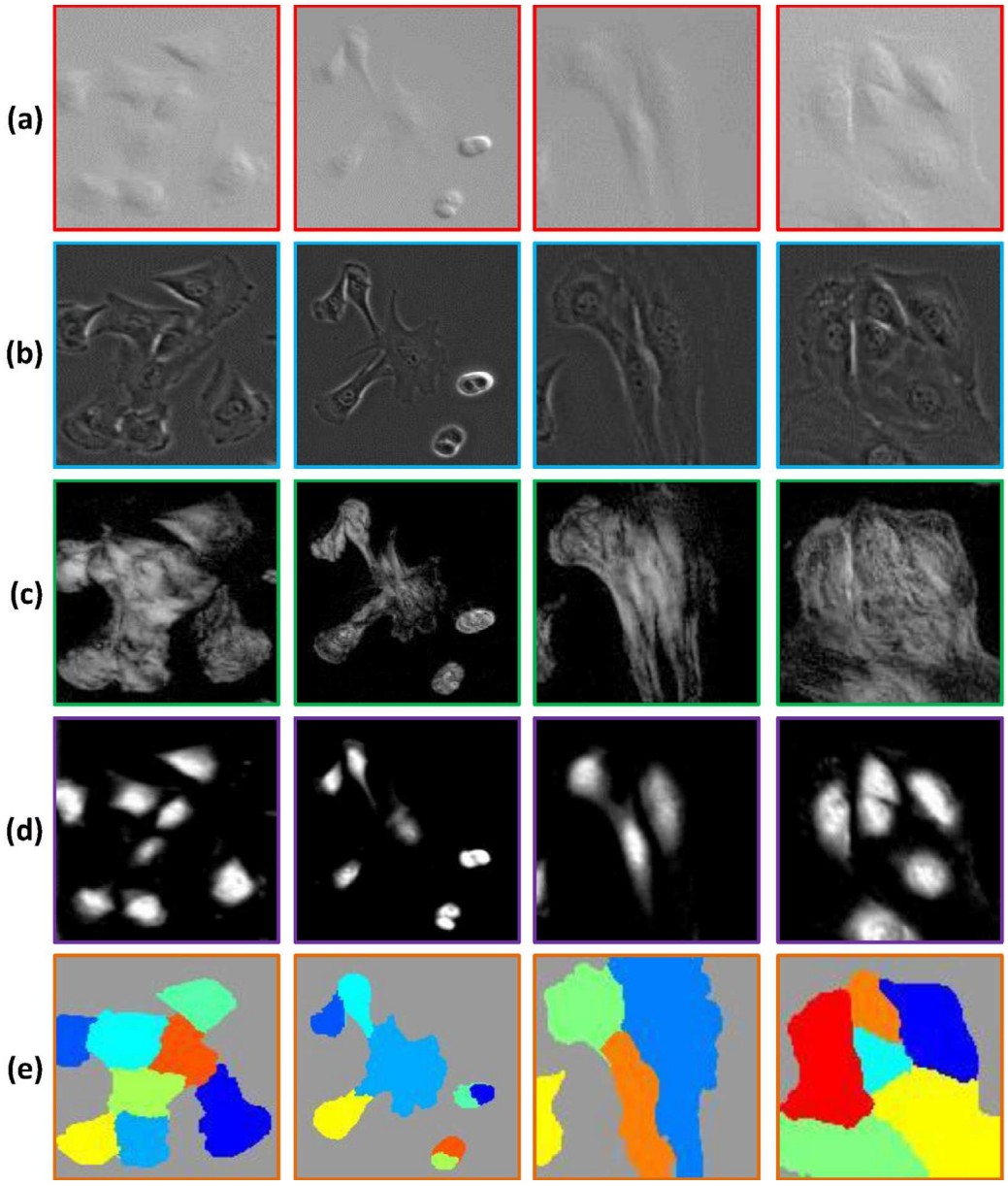

Fig. 16. Qualitative object-level cell segmentation evaluation. (a). The original DIC images. (b). The corresponding phase contrast images as a ground truth reference. (c). The restored DIC images by our restoration method. (d). The restoration results by preconditioning Li and Kanade (2009), which are the initial labeled pixel samples. (e). The object-level cell segmentation results.

Precision=TP/(TP+FP) and recall is defined as Recall=TP/(TP+FN). To quantitatively compare the performance, we compute the Area Under the recall-precision Curve (AUC). As summarized in Fig. 14(c), our proposed restoration algorithm greatly outperforms the other three approaches since we can restore cells' fine details in addition to the nucleus.

4.4. Advanced visualization

The proposed restoration method relies on motion magnification for restoring cells' fine structures, which means that our method pays more attention to the motion among a series of images rather than a single image. However, the stationary information restored from a single image might provide complement information to the restored details from motion magnification. This inspires us to combine the motion information from our restoration method with the restored stationary information from the previous work for the advanced visualization of DIC images. Preconditioning method Li and Kanade (2009) is a typical method that only depends on the target DIC image. Compared with the other works Kam (1998)Heise et al. (2005), preconditioning brings less artifacts and has better performance on restoring cell regions with large gradient signals of the phase variation. Fig. 15(e) shows the restoration results by equally adding the restoration results from our restoration method (Fig. 15(c)) into the preconditioned results (Fig. 15(d)). The advanced visualization is better than either motion magnification or preconditioning alone because it not only shows the hidden details of living cells such as the cytoplasm and cell membrane, but also presents the cell nuclei more clearly.

4.5. Application to object-level cell segmentation

Fig. 16 shows the qualitative object-level cell segmentation performance by the method proposed in Section 3. As illustrated in

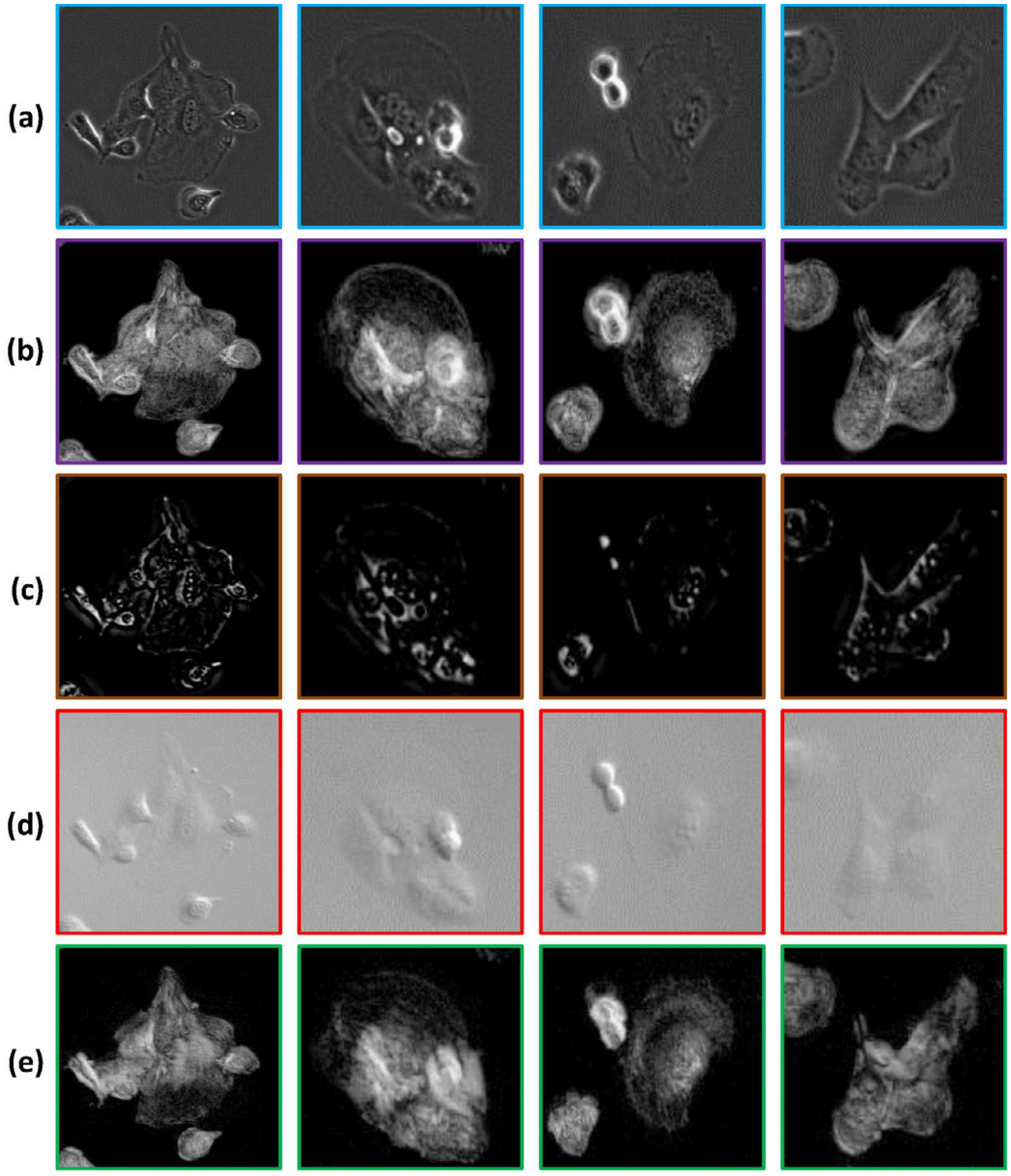

Fig. 17. Seeing the invisible details in phase contrast microscopy images. (a). The original phase contrast images. (b). The restoration results by the proposed restoration method applied to the phase contrast images. (c). The restoration results by sparsity regularized method proposed in Yin et al. (July 2012) applied to the phase contrast images. (d). The corresponding DIC images. (e). The restoration results by the proposed restoration method applied to the DIC images.

Fig. 16(c), the hidden details on cells can be revealed but the pixel-level restoration can not separate one cell from another when they are clustered. Taking the cell nuclei regions (Fig. 16(d)) obtained by the preconditioning method Li and Kanade (2009) as initial labeled pixel samples, we can compute the probability of the unlabeled pixels belonging to a specific cell class, based on the restoration results (Fig. 16(c)). Fig. 16(e) is the oject-level cell segmentation results where each cell can be accurately segmented even though they gather together as a cluster.

To quantitatively evaluate the object-level cell segmentation, we compute the Tanimoto coefficient (TC), which is defined as:

$$TC = \frac{area(C_{sc} \bigcap C_{gt})}{area(C_{sc} \bigcup C_{gt})} \tag{11}$$

where C_{sc} and C_{gt} are the segmented cell regions by the proposed object-level segmentation algorithm and ground truth annotated by humans, respectively. The average TC for dataset 1 is 0.89 and that for dataset 2 is 0.85. This object-level cell segmentation would be helpful to analyze cells' behavior and shape change over time.

4.6. Application to phase contrast microscopy images

Besides DIC microscopy, phase contrast microscopy Zernike (1955) is another popular non-invasive microscopy imaging modality, which converts the minute phase difference between waves traversing the biological specimen and those passing through the surrounding medium to a visible difference in image intensity. We have been using phase contrast images as ground truth references in this paper. In fact, both DIC and phase contrast microscopy have their own advantages and drawbacks (please refer to http://www.microscopyu.com/tutorials/java/phasedicmorph/index.html for the detailed comparison), so both of the two imaging modalities have been widely used by biologists for different biological experiments. Similar to

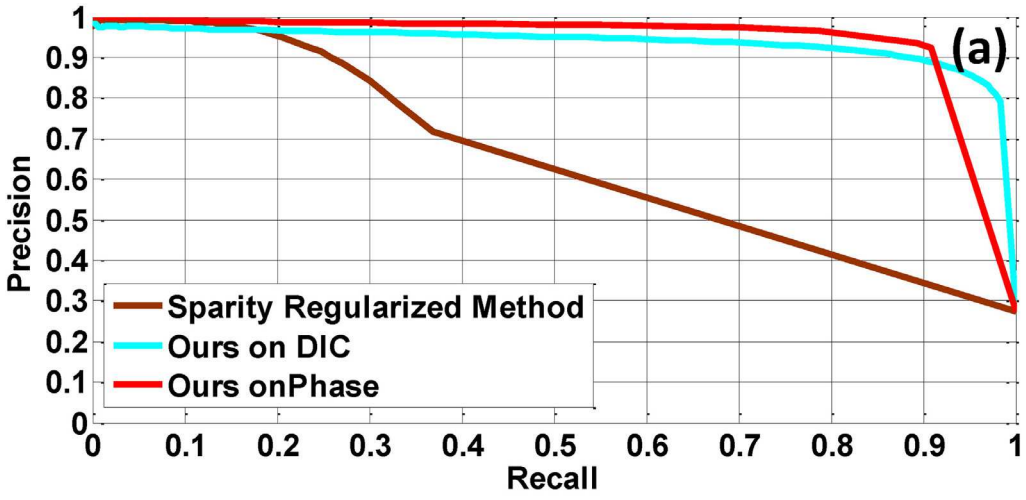

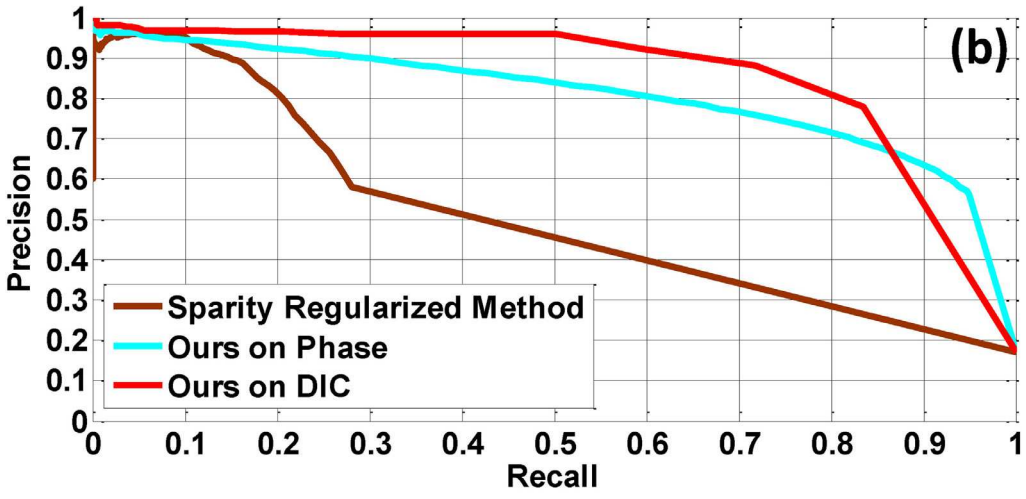

Dataset	(c). Area Under the Curve		
	Sparsity Regularized Method	Ours on Phase	Ours on DIC
Dataset 1	0.6536	0.9359	0.9438
Dataset 2	0.5113	0.8053	0.8577

Fig. 18. The recall vs. precision comparison among the sparsity regularized method Yin et al. (July 2012), our restoration method on DIC images and our restoration method on phase contrast microscopy images. (a). Comparison on dataset 1. (b). Comparison on dataset 2. (c). The area under the ROC curve.

DIC microscopy, phase contrast microscopy is also insensitive at regions having small differences of optical path length, such as the flat specimens which produce little contrast and often appear in the image at the same intensity level as the background. Thus, it is significant to study the possibility to apply our proposed method to phase contrast images as well. It is promising because our proposed method does not rely on the image formation process of microscopy images, which differs from our previous phase contrast restoration methods that depend on the microscopy imaging model Yin et al. (July 2012).

Fig. 17 shows the qualitative results by applying our proposed method to restore microscopy images. Fig. 17(b) and Fig. 17(e) show the restoration results of phase contrast images and DIC images by our restoration method, respectively. The restoration results on two imaging modalities are very similar, which indicates our method can successfully reveal the hidden details of cells in phase contrast images and obtain comparable performance as DIC images. Fig. 17(c) shows the restoration results by applying the sparsity regularized method proposed in Yin et al. (July 2012) to phase contrast images, which does not work well in these cases where the cells are spread out to the background and their intensities are similar to the background.

With the same evaluation method described in Section 4.3, we compare our restoration on phase contrast images with the previous sparsity regularized method Yin et al. (July 2012) and our restoration on corresponding DIC images. Fig. 18 summarizes the comparison among the three methods. The comparison between the sparsity regularized method Yin et al. (July 2012) and our method applied to phase contrast images indicates that our method improves the state-of-the-art with a large margin in the

phase contrast imaging modality. When applying our restoration method to both DIC and phase contrast imaging modalities, the AUCs for DIC images and phase contrast images are 0.9438 and 0.9359 for dataset 1, and 0.8577 and 0.8053 for dataset 2, respectively. The proposed method applied to DIC images achieves slightly better performance than that applied to phase contrast images.

5. Conclusion

In this paper, we propose a novel motion-based DIC image restoration algorithm. The gradient information in DIC images is magnified based on a Laplacian pyramid method. The tiny motion of each cell pixel is magnified by filtering a time-series of gradient-magnified DIC image signals on the pixel location using an ideal bandpass filter, while the intensity variation on the background pixels is attenuated. The motion information of a target image is further magnified by a weighted sum of a series of motion images from time-lapse image sequences. From our restored images, we can clearly observe the previously-invisible details in DIC images such as the cytoplasm and cell membrane. The restored images facilitate the cell segmentation greatly. Combining with the single-image-based restoration method which recovers the cell nuclei regions, our restoration based on a series of DIC images can visualize the full details of cell appearance. Furthermore, we demonstrate that the motion-based restoration method can be applied to other imaging modalities such as phase contrast microscopy to recover appearance details on cell regions that have similar intensities to the background in original images. Additionally, we also leverage the label propagation method in a supervised graph to obtain the object-level segmentation based on the pixel-level restoration results. In the future, we plan to explore cell image analysis tasks based on our restoration algorithm such as the cell shape dynamics during the cell proliferation process.

Acknowledgement

This work was supported by Intelligent Systems Center (ISC) and Center for Biomedical Science and Engineering (CBSE) at Missouri University of Science and Technology, and the National Science Foundation (NSF) CAREER Award IIS-1351049 and NSF EPSCoR grant IIA-1355406. Any opinions, findings, and conclusions or recommendations expressed in this material are those of the author(s) and do not necessarily reflect the views of the National Science Foundation.

The authors would like to thank Elmer Ker for motivating this work and helpful discussion. We highly appreciate the reviewers for the constructive comments to refine the paper.

Supplementary material

Supplementary material associated with this article can be found, in the online version, at 10.1016/j.media.2016.04.010

References

Ancuti, C., Ancuti, C.O., Haber, T., Bekaert, P., 2012. Enhancing underwater images and videos by fusion. IEEE Conference on Computer Vision and Pattern Recognition (CVPR).

Arnison, M.R., Cogswell, C.J., Smith, N.I., Fekete, P.W., Larkin, K.G., 2000. Using the hilbert transform for 3d visualization of differential interference contrast microscope images. J. Microsc. 199 (1), 79–84.

Arnison, M.R., Larkin, K.G., Sheppard, C.J.R., Smith, N.I., Cogswell, C.J., 2003. Linear phase imaging using differential interference contrast microscopy. J. Microsc. 214 (1), 7–12.

Banerjee, S., Scherer, N.F., Dinner, A.R., 2016. Shape dynamics of growing cell walls. Soft Matter 12, 3442–3450.

Carter, J.A., Hyland, C., Steele, R.E., Collins, E.M.S., 2016. Dynamics of mouth opening in hydra. Biophys. J. 110 (5), 1191–1201.

Ce, L., Sun, D., 2014. On bayesian adaptive video super resolution. IEEE Trans. Pattern Anal. Mach. Intell. 36 (2), 346–360.

Harris, G.M., Piroli, M.E., Jabbarzadeh, E., 2014. Deconstructing the effects of matrix elasticity and geometry in mesenchymal stem cell lineage commitment. Adv. Funct. Mater. 24 (16), 2396–2403.

Heise, B., Arminger, B., 2007. Some aspects about quantitative reconstruction for differential interference contrast (DIC) microscopy. Proc. Appl. Math. Mech. 7, 2150031–2150032.

Heise, B., Sonnleitner, A., Klement, E.P., 2005. DIC image reconstruction on large cell scans. Microsc. Res. Tech. 66 (6), 312–320.

Hennies, J., Bergeest, J.-P., Eck, S., Rohr, K., Worz, S., 2014. Cell Segmentation and Cell Splitting Based on Gradient Flow Tracking in Microscopic Images. Springer Berlin Heidelberg, pp. 409–414.

Jiang, W., Yin, Z., 2015. Restoring the invisible details in differential interference contrast microscopy images. In: the 18th International Conference on Medical Image Computing and Computer Assisted Intervention (MICCAI).

Kaakinen, M., et al., 2014. Automatic detection and analysis of cell motility in phasecontrast timelapse images using a combination of maximally stable extremal regions and kalman filter approaches. J. Microsc. 253 (1), 65–78.

Kam, Z., 1998. Microscopic differential interference contrast image processing by line integration (LID) and deconvolution. Bioimaging 6 (4), 166–176.

King, S.V., Libertun, A., Piestun, R., Cogswell, C.J., Preza, C., 2008. Quantitative phase microscopy through differential interference imaging. J. Biomed. Opt. 13 (2), 024020.

Li, K., Kanade, T., 2009. Nonnegative mixed-norm preconditioning for microscopy image segmentation. Information Processing in Medical Imaging(IPMI). Springer Berlin Heidelberg.

Li, K., Miller, E., Chen, M., Kanade, T., Weiss, L., Campbell, P., 2008. Cell population tracking and lineage construction with spatiotemporal context. Med. Image Anal. (MedIA) 12 (5), 546–566.

Li, M., Yin, Z., 2015. Co-restoring multimodal microscopy images. In: the 18th International Conference on Medical Image Computing and Computer Assisted Intervention (MICCAI).

Liu, K., Lienkamp, S. S., Shindo, A., Wallingford, J. B., Walz, G., Ronneberger, O., 2014. Optical flow guided cell segmentation and tracking in developing tissue. IEEE International Symposium on Biomedical Imaging (ISBI).

Murphy, D.B., 2001. Fundamentals of Light Microscopy and Electronic Imaging. John Wiley & Sons.

Neumann, B., Held, M., Liebel, U., Erfle, H., Rogers, P., Pepperkok, R., Ellenberg, J., 2006. High-throughput RNAi screening by time-lapse imaging of live human cells. Nat. Methods 3, 385–390.

Preza, C., 2000. Rotational-diversity phase estimation from differential-interference–contrast microscopy images. J. Opt. Soc. Am. A 17 (3), 415–424.

Shribak, M., LaFountain, J., Biggs, D., Inouè, S., 2008. Orientation-independent differential interference contrast (DIC) microscopy and its combination with orientation-independent polarization system. J. Biomed. Opt. 13 (1), 014011.

Su, H., Yin, Z., Huh, S., Kanade, T., Zhu, J., March 2016. Interactive cell segmentation based on active and semi-supervised learning. IEEE Trans. Med. Imag. 35 (3), 762–777.

Su, H., Yin, Z., Kanade, T., Huh, S., 2012. Phase contrast image restoration via dictionary representation of diffraction patterns. In: the 15th International Conference on Medical Image Computing and Computer Assisted Intervention (MICCAI).

Su, H., Yin, Z., Kanade, T., Huh, S., 2014. Interactive cell segmentation based on correction propagation. IEEE International Symposium on Biomedical Imaging (ISBI).

Van Munster, E.B., Vliet, L.J.V., Aten, J.A., 1997. Reconstruction of optical path length distributions from images obtained by a wide-field differential interference contrast microscope. J. Microsc. 188 (2), 149–157.

Wu, H.Y., Rubinstein, M., Shih, E., Guttag, J., Durand, F., Freeman, W., 2012. Eulerian video magnification for revealing subtle changes in the world. ACM Trans. Graph. 31 (4).

Yin, Z., Kanade, T., 2011. Restoring artifact-free microscopy image sequences. IEEE International Symposium on Biomedical Imaging (ISBI).

Yin, Z., Kanade, T., Chen, M., July 2012. Understanding the phase contrast optics to restore artifact-free microscopy images for segmentation. Med. Image Anal. (MedIA) 16 (5), 1047–1062.

Yin, Z., Ker, D., Kanade, T., 2011. Restoring DIC microscopy images from multiple ahear directions. Information Processing in Medical Imaging (IPMI). Springer Berlin Heidelberg.

Yin, Z., Li, K., Kanade, T., Chen, M., 2010. Understanding the optics to aid microscopy image segmentation. In: the 13th International Conference on Medical Image Computing and Computer Assisted Intervention (MICCAI).

Yin, Z., Su, H., Ker, E., Li, M., Li, H., 2014. Cell-sensitive microscopy imaging for cell image segmentation. In: the 17th International Conference on Medical Image Computing and Computer Assisted Intervention (MICCAI).

Yin, Z., Su, H., Ker, E., Li, M., Li, H., 2015. Cell sensitive phase contrast microscopy imaging by multiple exposures. Med. Image Anal. (MedIA) 25 (1), 111–121.

Yu, S.K., Liu, T.-K., Lin, S.-C., 2010. Height measurement of transparent objects by adopting differential interference contrast technology. Appl. Opt. 49 (14), 2588–2596.

Zernike, F., 1955. How I discovered phase contrast. Science 121, p345–p349.